Journal of Materials Science & Technology 129 (2022) 108–114

Contents lists available at ScienceDirect

Journal of Materials Science & Technology

journal homepage: www.elsevier.com/locate/jmst

Research Article

Integration of filter membrane and $Ca_2Nb_3O_{10}$ nanosheets for high performance flexible UV photodetectors

Yong Zhang[a,b,1], Fa Cao[b,1], Siyuan Li[b], Xinya Liu[b], Lixing Kang[c,*], Limin Wu[b,d,*], Xiaosheng Fang[b,*]

[a] School of Electronic and Information Engineering, Changshu Institute of Technology, Changshu 215500, China
[b] Department of Materials Science, Fudan University, Shanghai 200433, China
[c] Division of Advanced Materials Suzhou Institute of Nano-Tech and Nano-Bionics, Chinese Academy of Sciences, Suzhou 215123, China
[d] College of Chemistry and Chemical Engineering, Inner Mongolia University, Hohhot 010021, China

ARTICLE INFO

Article history:
Received 17 March 2022
Revised 24 April 2022
Accepted 25 April 2022
Available online 25 May 2022

Keywords:
UV photodetector
$Ca_2Nb_3O_{10}$ nanosheets
Filter membrane
Flexible

ABSTRACT

We report that the integration of filter membrane and $Ca_2Nb_3O_{10}$ nanosheets (FM@CNO) UV photodetector (UV PD) shows high performance and excellent flexibility. The $Ca_2Nb_3O_{10}$ nanosheets were prepared by a facile solid-state reaction and liquid exfoliation process. The $Ca_2Nb_3O_{10}$ nanosheets can be integrated into the pores of a filter membrane via a simple vacuum filtration method. The FM@CNO UV PD shows high performance under 300 nm light illumination at 5 V bias, including high responsivity (0.08 AW^{-1}), high detectivity (1.1×10^{12} Jones), high UV/visible rejection ratio (3.86×10^3) and fast speed (0.12/1.24 ms). Furthermore, the FM@CNO device exhibits excellent flexibility after many bending cycles. In addition, the FM@CNO array device was used as a pixel array detector for UV imaging. This work provides a novel approach to achieve high performance flexible PDs based on filter membrane and two dimensional materials.

© 2022 Published by Elsevier Ltd on behalf of The editorial office of Journal of Materials Science & Technology.

1. Introduction

Perovskite-type transition metal oxides have been investigated because they exhibit unique properties. Their layered derivatives, including Ruddlesden-Popper phase, Aurivillius phase and Dion-Jacobson phase, have been a research focus nowadays [1–3]. Among those layered perovskite derivatives, the group of Dion-Jacobson phase, with the general formula of $A'[A_{n-1}B_nO_{3n+1}]$ ($n>1$) covers a wide range of materials, including titanates, tantalates, niobates and solid solutions. The Dion-Jacobson derivatives exhibit a number of interesting properties, such as protonic/electronic conductivity, ferroelectricity and large specific surface area, which meet the demand of basic research and practical applications such as miniaturized electronic devices [4–6]. And of particular interest are two-dimensional (2D) nanostructures synthesized via the solution-processed exfoliation of layered bulk perovskites. Such 2D nanostructures are practically useful building blocks for assembling patterns and complex architectures, and provide various possibilities for many applications [7,8].

$KCa_2Nb_3O_{10}$ is a Dion-Jacobson phase layered perovskite, consists of a layer of K^+ ion and two adjacent layers of negatively charged NbO_6 octahedrons. Two dimensional $Ca_2Nb_3O_{10}$ (CNO) nanosheets can be synthesized via a simple solid-state reaction, proton-exchange, aqueous phase exfoliation process. The CNO nanosheets films have been proven to be a promising material for various traditional or late-model applications such as dielectric, ferroelectric, photocatalysis and optical applications [9–11]. In addition, the bandgap of CNO corresponds to the UV energy spectrum, therefore it may become a promising candidate for UV light detection. Until recently, we first reported 2D $Ca_2Nb_3O_{10}$ (CNO) and $Sr_2Nb_3O_{10}$ (SNO) nanosheets for high performance UV photodetectors (UV PDs), respectively [12,13]. The device based on an individual CNO nanosheet presents an ultrahigh responsivity of 1156 AW^{-1}. However, the development of high performance and flexible devices based on CNO nanosheets and well-selected substrates by a simple and low-cost technique is still lacking.

Recently, intelligent and integrated wearables are springing up in our daily lives with the great progress of science and technology, and have attracted wide attention in various fields such as health monitors, power supplies, optoelectronic devices and various sen-

* Corresponding authors.
E-mail addresses: lxkang2013@sinano.ac.cn (L. Kang), lmw@fudan.edu.cn (L. Wu), xshfang@fudan.edu.cn (X. Fang).
[1] Two authors contributed equally to this work.

https://doi.org/10.1016/j.jmst.2022.04.035
1005-0302/© 2022 Published by Elsevier Ltd on behalf of The editorial office of Journal of Materials Science & Technology.

sors [14–18]. An enormous challenge facing the design methods of wearable devices is the requirement of good flexibility and high performance. Among them, the rapid progress of photodetection techniques is becoming increasingly important in modern optoelectronic technology, in which the development of wearable devices plays a significant role. Considerable efforts have been made in search of high performance flexible PDs through elaborately planned fabrication methods, well-designed structures, and selection of suitable nanometer materials [19–23]. The general strategy to realize of the flexibility and portability of PDs is to develop a variety of flexible substrates. Chen et al. reported that the single microwire with a 3D porous structure is prepared via a femtosecond laser writing technique [24]. And the SiC microwires can be deposited directly on flexible substrate, and the obtained SiC UV devices has good flexibility and can work stably after bending 2000 times. However, ingenious methods are still needed to realize the integration of materials and substrates for high performance PDs with good flexibility.

Herein, the ultrathin CNO nanosheets were synthesized via a solid-state reaction, aqueous phase exfoliation process. After the vacuum filtration of CNO nanosheets colloidal suspension, the integration of filter membrane and CNO nanosheets (FM@CNO) is obtained with CNO nanosheets in its pores. The FM@CNO UV PDs show high performance at 5 V under 300 nm light illumination, including the high responsivity (0.08 AW^{-1}), high detectivity (1.1×10^{12} Jones), high UV/visible rejection ratio (3.86×10^{3}) and fast speed (0.12/1.24 ms). Furthermore, the FM@CNO UV PD exhibits excellent flexibility after many bending cycles. In addition, the FM@CNO array device was measured as an UV image sensor. This work provides a novel approach to achieve flexible and high performance PDs based on filter membrane and two dimensional materials.

2. Experimental

2.1. Synthesis of $Ca_2Nb_3O_{10}$ nanosheets

The calcination-exfoliation process was carried out in our previous work.[12] Typically, the mixture of K_2CO_3, $CaCO_3$, Nb_2O_5 with the molar ratio of K:Ca:Nb = 1.1:2:3 was fully ground and was calcinated at 1273 K for 10 h in air. Then the $KCa_2Nb_3O_{10}$ was prepared after another calcination for 12 h at 1473 K after secondary ground. An excess amount of K_2CO_3 was used because the loss of alkali metal carbonate was compensated at high temperature. The proton-exchange steps which replaces K^+ with H^+ was carried out by immersing 0.5 g $KCa_2Nb_3O_{10}$ sample in 5 M HNO_3 for 5 days during which the nitric acid solution was renewed daily. The powder was washed several times and dried in air before being dispersed in an aqueous solution containing equimolar amounts of hydroxide (TBAOH). The $Ca_2Nb_3O_{10}$ nanosheets were exfoliated by slowly shaking the solution for 7 days. The unexfoliated $Ca_2Nb_3O_{10}$ sediment was removed and $Ca_2Nb_3O_{10}$ nanosheets were washed and collected by centrifugation. Finally, the $Ca_2Nb_3O_{10}$ nanosheets were dispersed in aqueous solution for further use. The whole experimental process was completed in the atmospheric environment. Therefore, the $Ca_2Nb_3O_{10}$ nanosheets have excellent stability to atmosphere, temperature, acid and alkali solutions.

2.2. Preparation of filter membrane and $Ca_2Nb_3O_{10}$ nanosheets (FM@CNO)

The integration of filter membrane and CNO nanosheets is prepared by vacuum filtration of CNO nanosheets colloidal suspension. After the removal of the upper CNO film, the lower filter membrane with CNO nanosheets in its pores (FM@CNO) is obtained. This integration of FM@CNO provides the possibility for flexible UV photodetecting applications.

2.3. Characterization and photoelectric measurements

The morphology of CNO nanosheets were conducted by field-emission scanning electron microscopy (Zeiss Sigma). An atomic force microscope measurement was observed on a Bruker atomic force microscope. High-resolution morphology of $Ca_2Nb_3O_{10}$ nanosheets were investigated by transmission electron microscope (FEI Tecnai F30). The crystal structure of CNO samples was characterized by a Bruker D8-A25 diffractometer. The GIXRD was performed on a Rigaku Smartlab 9 diffractometer. The UV-vis transmission spectroscopy was measured by a UV-vis spectrophotometer (Hitachi U-3900H).

The mask was employed for patterning of Cr/Au electrode contacts to fabricate the FM@CNO PDs. All the photoelectric performance was characterized by a program-controlled semiconductor characterization system (Keithley 4200, USA). A quick response system is measured on a digital oscilloscope (Tektronix DPO 5140B) equipped with a 355 nm pulsed laser source. The imaging test method is to block the T-shaped template between the light source and the device, and measure the light and dark current of each pixel one by one. The measured data were then projected into a 2D mapping diagram. All measurements were conducted in the atmosphere at room temperature.

3. Results and discussion

The $Ca_2Nb_3O_{10}$ (CNO) nanosheets are synthesized by a solid-state reaction, proton exchange in nitric acid, shaking-exfoliation in alkali solution. The scanning electron microscopy technique (SEM) is employed to observe the corresponding products, as shown in Fig. 1(a–c). After a two-step calcination, the $KCa_2Nb_3O_{10}$ (KCNO) product is observed from the SEM image in Fig. 1(a), and the lateral grain size of the KCNO can reach ten micron scale. It possesses a layered structure, leaving space for next intercalation and exfoliation. Then the $HCa_2Nb_3O_{10}$ (HCNO) product is prepared by replacing K^+ of KCNO product with H^+ in nitric acid, revealing a good layered structure, as shown in Fig. 1(b). Finally, the CNO nanosheets are successfully obtained by a slowly shaking-exfoliation step, in which the H^+ can be replaced by TBA^+ in TBAOH solution, as shown in Fig. 1(c). The lateral size of CNO nanosheets ranges from 200 to 1000 nm. And the size of CNO nanosheets can be screened by centrifugation at different speeds to obtain uniform sizes. The products of low-speed centrifugation are removed, and the products of high-speed centrifugation are used to fabricate devices. Meanwhile, according to the height profiles from the atomic force microscope image (AFM) in Fig. 1(d). The thickness of exfoliated single-layer CNO nanosheets is measured as 1.8 nm, which may contain the chain length of TBA^+ molecules. The thickness of a single-layer CNO nanosheet with three NbO_6 slabs is approximately 1.5 nm, and is close to the theoretical value of 1.45 nm [25]. Therefore, 2D single-layer or few-layers CNO nanosheets are achieved successfully, and can be dispersed in deionized water with good stability. This CNO nanosheets colloidal suspension is convenient for fabricating various optoelectronic devices.

The morphology, structure and elemental composition of CNO nanosheets are measured by transmission electron microscopy pattern (TEM). As shown in Fig. 1(e), the lateral size of the CNO nanosheets is clearly observed in low-magnification TEM. As seen in Fig. 1(f), the high-resolution TEM (HRTEM) image exhibits the interplanar distance along the two vertical directions are both calculated to be 0.38 nm, which corresponds to the (010) and (100) planes of CNO nanosheet. The selected-area electron diffraction

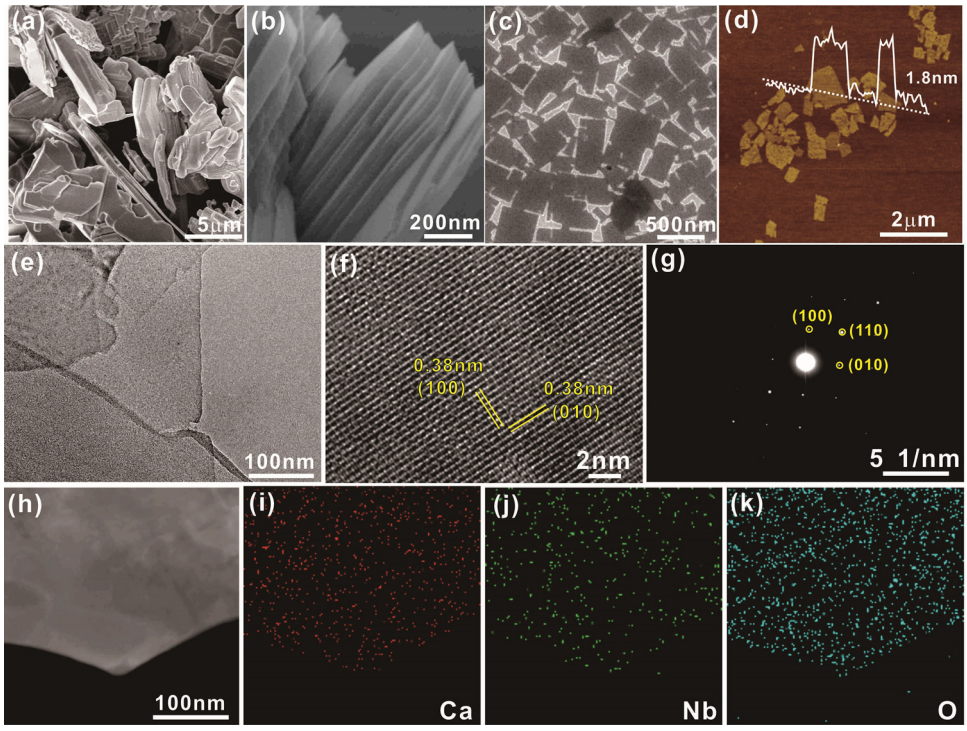

Fig. 1. Morphology and structure of CNO nanosheets. (a–c) SEM images of KCNO sample (a), HCNO sample (b) and CNO nanosheets (c). (d) AFM image of CNO nanosheets and insert exhibits the height profile. TEM image (e), HRTEM image (f) and SAED pattern (g) of CNO nanosheet. (h) TEM image of CNO nanosheet and the corresponding EDS mapping diagrams of Ca (i), Nb (j) and O (k) elements, the scale is uniform.

(SAED) pattern with the high crystallinity are indexed as (010) and (100) planes of CNO nanosheet in Fig. 1(g). The structure of the single-layer CNO nanosheet with three NbO_6 slabs share corners to construct a unilamellar sheet, where the *c*-axis is along [001] zone axis direction. Furthermore, the energy-dispersive X-ray spectroscopy mapping pattern (EDS) is investigated to analyze the elements distribution of CNO sheets. Fig. 1(h–k) shows the typical EDS mapping results of the CNO nanosheet. It can be seen that Ca (Fig. 1(i)), Nb (Fig. 1(j)) and O(Fig. 1(k)) are evenly distributed in the CNO nanosheets. Note that the nanosheets with few octahedral layers are easily damaged by the electron beam with the prolongation of the sampling time. Therefore, the sampling time is short and the number of sampling points is small. Single-layer or few-layer CNO nanosheets have small sizes and ultrathin thicknesses, which is conducive to their combination with various substrates.

To determine the phase structure of products during the preparation process, the X-ray diffraction pattern (XRD) is utilized for products after high temperature calcination and proton-exchange, respectively. And the grazing incidence X-ray diffraction measurement (GIXRD) is carried out for the exfoliated CNO nanosheets because of the ultrathin thickness. As displayed in Fig. 2(a–c), during the three experimental steps the crystal phase of products changes substantially. For product synthesized by calcination as seen in Fig. 2(a), the strong peaks at 32.9, 31.3, 29.4, 23.1, 12.0 and 5.8° match well with the standard data of (221), (207), (206), (200), (004) and (001) planes of $KCa_2Nb_3O_{10}$ (PDF#35-1294). After the exchange process, the four strongest peaks centered at 32.9°, 29.7°, 23.1° and 6.1° are observed in Fig. 2(b), corresponding with the (110), (103), (100) and (001) planes of $HCa_2Nb_3O_{10}$ (PDF#40-0884). After the exfoliation process, the GIXRD measurement of CNO sheets present obvious diffraction peaks at 28.4°, 23.1°, 10.9° and 5.4°, corresponding to (103), (100), (002) and (001) planes of $HCa_2Nb_3O_{10}{\cdot}1.5H_2O$ (PDF#39-0915) in Fig. 2(c). And the broad diffraction peaks of CNO nanosheets indicate the decrease of the crystal size along the *c* axis. The optical property of CNO nanosheets is further measured. The CNO nanosheets exhibit little absorption in the visible range and a sharp absorption edge around 300 nm, according to the UV-vis absorption spectrum in Fig. 2(d). As presented in Fig. 2(e), the optical bandgap could be calculated to be 3.84 eV by the Tauc plots. The wide bandgap of the CNO nanosheets makes it feasible for fabricating UV PDs. In our previous work, CNO nanosheets are coated on quartz substrate to form film-based device, which shows excellent photoelectric properties. Herein we investigate their applications in flexible photoelectric devices.

The CNO nanosheets were obtained successfully through a simple calcination and exfoliation process. Due to the existence of water-soluble surface ligands (TBA^+), the CNO nanosheets have good stability and dispersion in deionized water for one year. Fig. 3(a) shows the schematic diagram of the preparation process for the FM@CNO. In order to obtain flexible free-standing CNO film, the composite of CNO nanosheets film and filter membrane can be obtained by vacuum filtration of CNO nanosheets colloidal suspension for one hour. After overnight drying in a desiccator, the upper free-standing CNO film is easily removed from the filter membrane by using tweezers carefully, as shown in Fig. 3(b). However, the upper free-standing CNO film shows poor flexibility. Unexpectedly, it is found that the lower filter membrane is observed to have CNO nanosheets with nanometer lateral scale in its pores, as exhibited in Fig. 3(c). It can be observed clearly that a considerable number of CNO nanosheets are tightly adsorbed on the filter membrane surface. In high-resolution SEM images, a large number of nanosheets with different sizes are filled in the pores of the filter membrane by vacuum filtration, as seen in Fig. 3(d). Due to the small scales of the ultrathin sheets, the flexible CNO nanosheets can adjust their shapes to match the pore size of the filter membrane. This integration of CNO nanosheets and filter membrane is simplified and named the FM@CNO. After stripping the upper CNO nanosheets film, the lower FM@CNO was obtained successfully, and the CNO nanosheets were closely stacked and contacted

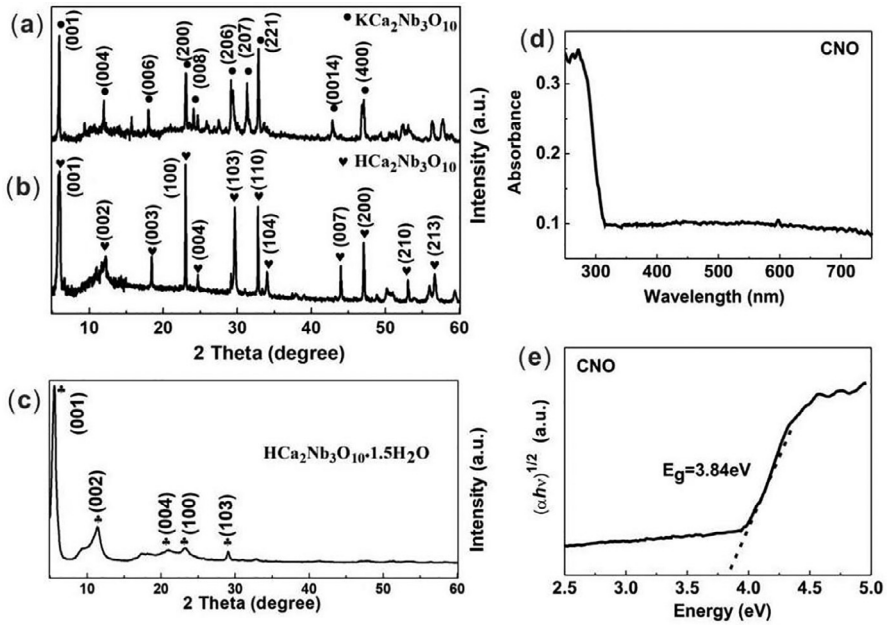

Fig. 2. (a, b) XRD patterns of samples after calcination (a) and proton-exchange (b); (c) GIXRD pattern of CNO nanosheets. (d, e) UV-vis absorption spectrum (d) and the corresponding Tauc curve (e) of obtained CNO nanosheets.

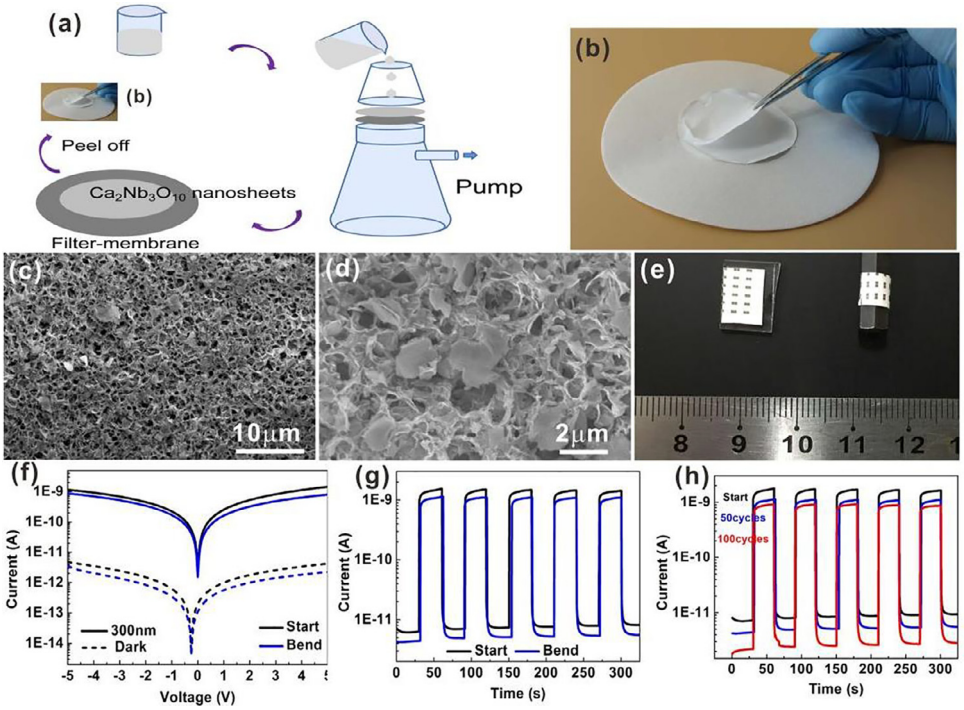

Fig. 3. (a) Schematic diagram of preparation process for FM@CNO. (b) Photograph of the upper CNO film and the lower FM@CNO. (c, d) SEM images of FM@CNO with different magnification. Photograph (e), *I-V* curves (f) and *I-t* curves (g) of FM@CNO PDs in the initial state and bending state. The *I-t* curves of FM@CNO PD after various bending cycles.

with each other in the pores of the filter membrane. This unique architecture of FM@CNO provides the possibility for flexible UV photodetecting properties. This architecture is different from other paper-based photodetectors [26,27]. Through this simple filtration-stripping process, we provide a novel architecture system to integrate 2D materials and filter membranes for future wearable electronic devices.

The FM@CNO PD is fabricated via deposition of Cr/Au electrodes by using mask. Further the photodetecting performance of obtained CNO@FM device is studied using a two-probe method at room temperature. As shown in Fig. 3(e), the performance of FM@CNO device is measured under initial (the plane state) and bending conditions, respectively. And the schematic device structures are simply illustrated in Fig. S1. The uniformity of the FM@CNO UV PDs can be qualitatively explained by a vacuum filtration time. The current-time (*I-t*) curves of FM@CNO UV PDs are measured in different filtration time (0.5, 1.0 and 2.0 h). As shown in Fig. S2, the FM@CNO devices demonstrate good uniformity. Therefore, one hour of filtration time is enough to prepare the high performance FM@CNO PDs. Fig. 3(f) exhibits the current

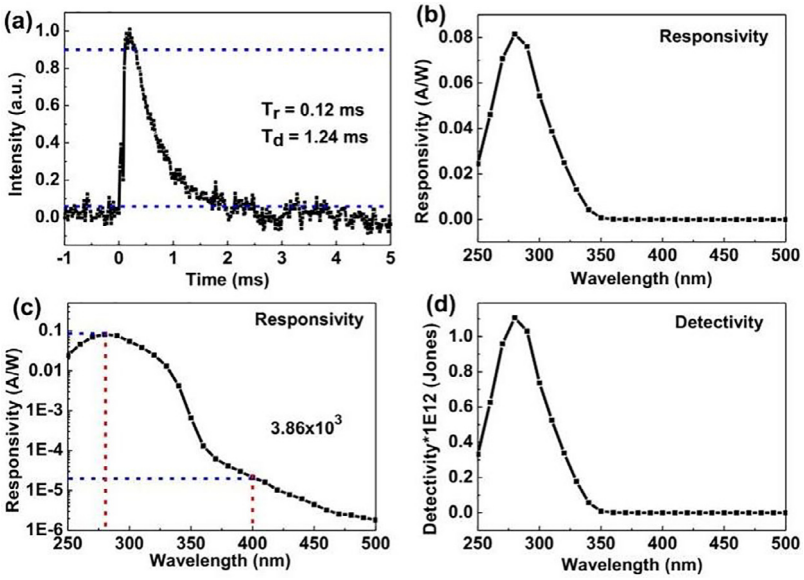

Fig. 4. Photodetecting performance of FM@CNO device at 5 V at 300 nm. (a) Normalized pulse response, (b, c) responsivity and (d) detectivity for the FM@CNO device.

versus voltage (*I-V*) characteristics of the FM@CNO device in the dark condition and upon 300 nm light irradiation in a logarithmic plot. For initial and bending state of the FM@CNO devices, the great enhancement in photocurrents are all observed clearly. The photocurrents can reach 1 nA under 300 nm light irradiation, which are all much higher than dark currents at 5 V bias. The photocurrents of the devices are as high as about 350 times the dark currents at the bias of 5 V. It is noteworthy that the photocurrent and the dark current of the initial FM@CNO PD are all slightly higher than that of the bending FM@CNO PD at 5 V. Hence the FM@CNO device demonstrates a good light response in the UV region under the initial and bending conditions. The repeatability is significant parameter to evaluate a device. Fig. 3(g) exhibits the *I-t* features of the initial and bending FM@CNO devices at 5 V with a periodic 300 nm light irradiation. The *I-t* curves present that the initial and bending FM@CNO devices exhibit a reproducible and rapid photo-response without any noticeable delay. For the initial FM@CNO PD, the current rapidly increases to 1.5 nA and rapidly decrease to its initial value of 7.5 pA as the UV light is switched on and off. For the bending FM@CNO device, the current increases quickly to the original value of 1.0 nA and declines quickly to the original value of 5.4 pA as the UV light is turned on and off. Obviously, the initial FM@CNO PD exhibits higher photocurrent and dark current than those of the bending FM@CNO device. The on/off ratio can be described as the ratio of photocurrent to dark current (I_{ph}/I_d) of a device. The on-off ratios of the initial and bending FM@CNO devices are calculated to be 200 and 185, respectively. In addition, the linear *I-V* curves of the FM@CNO PD in dark and light illumination are exhibited in Fig. S3, respectively. The working principle of the device may be clarified through a simplified energy band diagram. In the dark condition, the contact barriers mainly determine the electron transport in the channel, leading the device in an equilibrium state. Under 300 nm light irradiation, the photocurrent rises linearly and the sample Fermi level down shifts, producing to a high energy barrier between two contact interfaces. In that case, the photo-generated electron-hole pairs would occupy the channel, which demonstrates a high sensitivity to UV light illumination.

Recently optoelectronic devices with flexible characteristics have experienceded fast development. The flexible FM@CNO device with large size is facilely fabricated by a simple filtration process without any extra additive. As indicated in Fig. 3(h), the *I-t* curves of the FM@CNO PD with a certain bending radian are measured after various bending circles at 5 V bias under 300 nm light irradiation. A cycle means that the device bends to a certain radian by hand from the initial state, and then returns to the initial state. As the UV light is switched on and off, the photocurrents of the FM@CNO device with different bending circles all exhibit high stability and repeatability. As the UV light is switched on and off, and the currents rapidly increase to 1.6 nA, 1.0 nA and 0.9 nA, and then rapidly decay to 8.8 pA, 5.4 pA and 2.6 pA, respectively. The corresponding on-off ratios are calculated as 182, 185 and 350 separately. After 100 bending cycles, the cross-linking and stacking CNO nanosheets in the pores of filter membrane may be damaged, which may restrict the transport of photocarriers between adjacent sheets. The resistance of FM@CNO PD increases and the corresponding photocurrent and dark current decrease with increasing the bending cycles. These results reveal that the FM@CNO devices still maintains excellent photoelectric properties after many bending cycles. Therefore, this PD indicates great prospect for operation in wearable electronic devices.

The four key parameters, i.e. response speed (T_r/T_d), spectral responsivity (R_λ), specific detectivity (D^*) and UV/visible rejection ratio (R_{280}/R_{400}), are investigated to characterize the performance of the FM@CNO device. The rise time (T_r) and the decay time (T_d), are described as time when the photocurrent rises from 10% to 90% of its peak and the photocurrent falls from 90 to 10% of its peak, respectively. The spectral responsivity (R_λ) is described as photocurrent per unit of incident light power, indicating how efficiently a PD responds to optical signals. The spectral detectivity (D^*, The unit is Jones) proves the ability to detect weak light signals from a noise background. The responsivity and specific detectivity can be expressed as the following equations:

$$R_\lambda = \frac{I_{ph} - I_d}{P_\lambda S} \quad (1)$$

$$D^* = \frac{R_\lambda}{(2eI_d/S)^{1/2}} \quad (2)$$

where I_d and I_{ph} are the dark current and photocurrent, e and λ are the electronic charge and the wavelength of irradiation light, S and P_λ represent the effective area under UV light irradiation and the light power density, respectively. A fast response measurement system is employed to calculate the accurate time of the FM@CNO

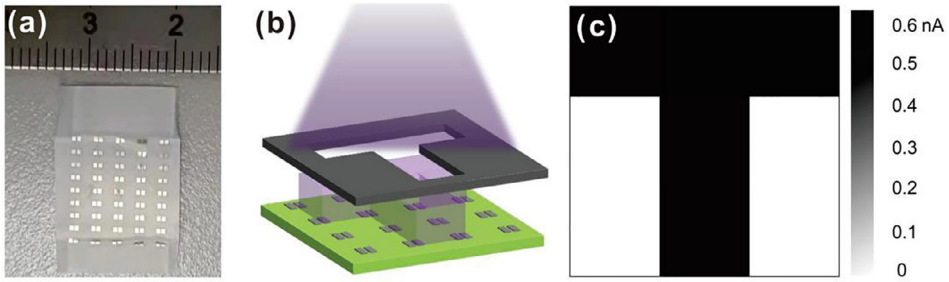

Fig. 5. (a) Photograph of FM@CNO array device. (b) Schematic diagram of the imaging test for the FM@CNO device. (c) Photocurrent uniformity of 3×3 FM@CNO device pixels, and image-sensing profiles of "T" under 300 nm illumination.

PD utilizing a pulsed laser. Fig. 4(a) exhibits the normalized curve of this device as a function of time under pulse response. The rise time and the decay time are measured to be 0.12 ms and 1.24 ms for the FM@CNO PD at 5 V, respectively. Fig. 4(b) and (d) demonstrate the responsivity and the specific detectivity of the FM@CNO PD with an incident light wavelength ranging from 500 to 250 nm at 5 V, respectively. As shown in Fig. 4(b), the maximum responsivity of FM@CNO PD is 0.08 AW^{-1} at 280 nm light irradiation, indicating a high photodetection for signals in the ultraviolet region. As seen in Fig. 4(c), the UV/visible rejection ratio of this device (R_{280}/R_{400}) is calculated as 3.86×10^3, revealing high spectral selectivity in visible blind area. Due to the small irradiation area and suppressed dark current, so the detectivity of this FM@CNO PD presents a maximum value of 1.1×10^{12} Jones (Fig. 4(d)).

Furthermore, the ability of the FM@CNO device for recording the image information under 300 nm light irradiation was investigated. Fig. 5(a) shows the photograph of the FM@CNO array devices. Fig. 5(b) demonstrates the schematic diagram of the imaging test and the image sensing array (3×3 pixels) by employing one detector for each pixel. Fig. 5(c) shows the photocurrent of 3×3 FM@CNO device pixels, demonstrating the excellent photocurrent uniformity, which is key for achieving high quality images. The sign with a hollow letter (T) was placed between the light source and the device array. The clear outlines of “T”were achieved by illuminating the sign with 300 nm light. These results suggest FM@CNO devices have potential applications in UV light imaging [28–30]. In addition, the CNO nanosheets and the filter membrane both have good stability. In brief, the fabrication process of FM@CNO photodetecting devices is simple, reproducible, cost-effective and environmentally friendly. And the FM@CNO devices show superior performance, excellent flexibility, and potentially extensible functionality. Therefore, FM@CNO devices may be a promising candidate for flexible optoelectronic devices in practical applications.

4. Conclusion

In summary, the $Ca_2Nb_3O_{10}$ nanosheets were prepared through a simple solid-state reaction, proton-exchange, exfoliation process. The $Ca_2Nb_3O_{10}$ nanosheets can be integrated into the pores of the filter membrane via a simple vacuum filtration method. The FM@CNO UV PD shows high performance under 300 light illumination, including high photocurrent (0.08 AW^{-1}), high detectivity (1.1×10^{12} Jones) and fast speed (0.12/1.24 ms). Furthermore, the FM@CNO device exhibits excellent flexibility after many bending cycles. In addition, the FM@CNO array device was used as a pixel array detector for UV imaging. This work provides a novel approach to achieve high performance photodetectors based on filter membrane and two dimensional materials.

Acknowledgments

The work was financially supported by the National Key R&D Program of China (No. 2017YFA0204600), the Inner Mongolia Talent Fund, the National Natural Science Foundation of China (Nos. 51872050 and 12061131009) and the Science and Technology Commission of Shanghai Municipality (Nos. 21520712600 and 19520744300).

Supplementary materials

Supplementary material associated with this article can be found, in the online version, at doi:10.1016/j.jmst.2022.04.035.

References

[1] W. Tian, H.P. Zhou, L. Li, Small 13 (2017) 1702107.
[2] D.X. Ji, S.H. Cai, T.R. Paudel, H.Y. Sun, C.C. Zhang, L. Han, Y.F. Wei, Y. Zang, M. Gu, Y. Zhang, W.P. Gao, H.X. Huyan, W. Guo, D. Wu, Z.B. Gu, E.Y. Tsymbal, P. Wang, Y.F. Nie, X.Q. Pan, Nature 570 (2019) 87–90.
[3] A.G. Ricciardulli, S. Yang, J.H. Smet, M. Saliba, Nat. Mater. 20 (2021) 1325–1336.
[4] T. Oshima, S. Nishioka, Y. Kikuchi, S. Hirai, K.I. Yanagisawa, M. Eguchi, Y. Miseki, T. Yokoi, T. Yui, K. Kimoto, K. Sayam, O. Ishitani, T.E. Mallouk, K. Maeda, J. Am. Chem. Soc. 142 (2020) 8412–8420.
[5] B.W. Li, M. Osada, Y.H. Kim, Y. Ebina, K. Akatsuka, T. Sasaki, J. Am. Chem. Soc. 139 (2017) 10868–10874.
[6] S. Ida, C. Ogata, M. Eguchi, W.J. Youngblood, T.E. Mallouk, Y. Matsumoto, J. Am. Chem. Soc. 130 (2008) 7052–7059.
[7] L. Hu, M. Chen, X.S. Fang, L. Wu, Chem. Soc. Rev. 41 (2012) 1350.
[8] Y. Bekenstein, B.A. Koscher, S.W. Eaton, P. Yang, A.P. Alivisatos, M.S. Khan, M. Osada, L. Dong, Y.H. Kim, Y. Ebina, T. Sasaki, ACS Appl. Mater. Interfaces 13 (2021) 1783–1790.
[9] L. Nurdiwijayanto, H. Nishijima, Y. Miyake, N. Sakai, M. Osada, T. Sasaki, T. Taniguchi, Nano Lett. 21 (2021) 7044–7049.
[10] T. Taniguchi, S.S. Li, L. Nurdiwijayanto, Y. Kobayashi, T. Saito, Y. Miyata, S. Obata, K. Saiki, H. Yokoi, K. Watanabe, T. Taniguchi, K. Tsukagoshi, Y. Ebina, T. Sasaki, M. Osada, ACS Nano 13 (2019) 11214–11223.
[11] T. Oshima, D. Lu, O. Ishitani, K. Maeda, Angew. Chem. Int. Ed. 54 (2015) 2736–2740.
[12] Y. Zhang, S. Li, Z. Li, H. Liu, X. Liu, J. Chen, X.S. Fang, Nano Lett. 21 (2021) 382–388.
[13] S.Y. Li, Y. Zhang, W. Yang, H. Liu, X.S. Fang, Adv. Mater. 32 (2020) 1905443.
[14] Y.H. Chen, L.X. Sua, M.M. Jiang, X.S. Fang, J. Mater. Sci. Technol. 105 (2022) 259–265.
[15] T.Q. Trung, N.E. Lee, Adv. Mater. 28 (2016) 4338.
[16] J. Wang, S. Li, F. Yi, Y. Zi, J. Lin, X. Wang, Y. Xu, Z.L. Wang, Nat. Commun. 7 (2016) 12744.
[17] X.J. Xu, J.X. Chen, S. Cai, Z.H. Long, Y. Zhang, L.X. Su, S.S. He, C.Q. Tang, P. Liu, H.S. Peng, X.S. Fang, Adv. Mater. 30 (2018) 1803165.
[18] H.L. Tai, Z.H. Duan, Y. Wang, S. Wang, Y.D. Jiang, ACS Appl. Mater. Interfaces 12 (2020) 31037.
[19] J.M. Hu, S.Y. Yang, Z.H. Zhang, H.L. Li, C.P. Veeramalai, M. Sulamana, M.I. Saleema, Y. Tang, Y.R. Jiang, L.B. Tang, B.S. Zou, J. Mater. Sci. Technol. 68 (2021) 216–226.
[20] L. Zhang, N.M. Li, Q.C. Ma, J.H. Ding, C. Chen, Z.C. Hua, W.W. Zhao, Y.F. Li, H.H. Feng, M.Y. Li, H.J. Ji, J. Mater. Sci. Technol. 110 (2022) 65–72.
[21] J.K. Song, M.S. Kim, S. Yoo, J.H. Koo, D.H. Kim, Nano Res. 14 (2021) 2919–2937.
[22] S. Cai, X.J. Xu, W. Yang, J.X. Chen, X.S. Fang, Adv. Mater. 31 (2019) 1808138.
[23] S.Y. Liang, Y.Z. Dai, G. Wang, H. Xia, J.H. Zhao, Nanoscale 12 (2020) 23200.
[24] J.X. Chen, Z.L. Li, F.L. Ni, W.X. Ouyang, X.S. Fang, Mater. Horiz. 7 (2020) 1828–1833.

[25] Y.H. Kim, H.J. Kim, M. Osada, B.W. Li, Y. Ebina, T. Sasaki, ACS Appl. Mater. Interfaces 6 (2014) 19510–19514.
[26] Y. Zhang, W.X. Xu, X.J. Xu, W. Yang, S.Y. Li, J.X. Chen, X.S. Fang, Nanoscale Horiz. 4 (2019) 452–456.
[27] S. Cai, C.L. Zuo, J.Y. Zhang, H. Liu, X.S. Fang, Adv. Funct. Mater. 31 (2021) 2100026.
[28] W.D. Song, J.X. Chen, Z.L. Li, X.S. Fang, Adv. Mater. 33 (2021) 2101059.
[29] J.X. Chen, X.Y. Liu, Z.Q. Li, F. Cao, X. Lu, X.S. Fang, Adv. Funct. Mater. 32 (2022) 2201066.
[30] C. Xie, X.T. Lu, Y. Liang, H.H. Chen, L. Wang, C.Y. Wu, D. Wu, W.H. Yang, L.B. Luo, J. Mater. Sci. Technol. 72 (2021) 189–196.